I&EC research
Industrial & Engineering Chemistry Research
pubs.acs.org/IECR
Article

Comparison between Bi_2WO_6 and TiO_2 Photoanodes in Dye-Sensitized Solar Cells: Experimental and Computational Studies

Amin Reza Zolghadr,* Omid Estakhr, Maryam Heydari Dokoohaki, and Hadi Salari*

Cite This: *Ind. Eng. Chem. Res.* 2021, 60, 12292−12306
Read Online
ACCESS | Metrics & More | Article Recommendations | Supporting Information

ABSTRACT: Dye-sensitized solar cells (DSSCs) demonstrate a clean and cheap technology to harness solar energy efficiently and have been studied in a large scale for safe and reliable energy supply. This research focuses on the experimental and computational study of DSSCs based on a different and novel metal oxide, bismuth tungstate (Bi_2WO_6), semiconductor as an electron conductor. This work is divided into four main topics: (1) the search for an appropriate Bi_2WO_6 nanostructure for better dye absorption, (2) comparison between Bi_2WO_6 and TiO_2 as photoanodes, (3) the impact of the semiconductor morphology on the performance of DSSCs, and (4) the study of the structural and dynamical properties of the dye solution and also the electrolyte mixture near electrodes in DSSCs. This study pointed out the poor properties of ruthenium-complex dye as sensitizers for Bi_2WO_6 and the great effect of Bi_2WO_6 surface charge on dye adsorption. The best performance of Bi_2WO_6 DSSC was obtained for morphologies synthesized at pH = 1, which can be attributed to the less negative surface charges of Bi_2WO_6 nanoparticles. Another important part of this paper was devoted to study the electrolyte distribution between anode and cathode surfaces for both TiO_2 and Bi_2WO_6 DSSCs. To our knowledge, acetonitrile-based electrolyte interactions with the Bi_2WO_6 photoanode have not been explored to date.

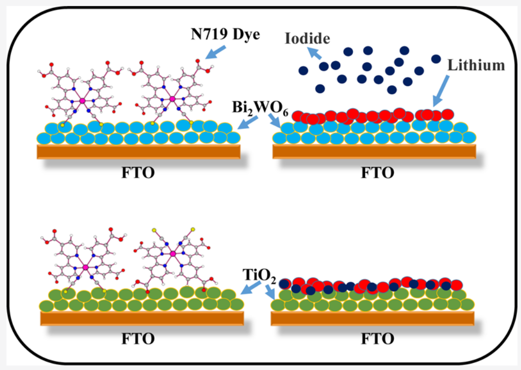

1. INTRODUCTION

Limited fossil energy resources and problems with greenhouse gas emissions highlight the need to pay more attention to renewable energy.[1] Solar energy is one of the largest sources of energy in the world, among renewable energy sources. The solar energy emitted by the sun to the earth every hour is more than the total energy consumed by the earth's inhabitants during a year.[2,3] Recently, dye-sensitized solar cells (DSSCs) have received more consideration, owing to their easy manufacturing process, low manufacturing costs, and low environmental pollution. DSSCs are composed of a dye-sensitized photoanode, an electrolyte, and a platinum-coated conductive glass as the counter electrode.[4−6] When Grätzel introduced the concept of DSSCs in 1991, much research was begun to find the optimal materials for better DSSC performance.[7]

A dye as a photosensitizer needs appending groups ($-SO_3H$, $-COOH$, $-H_2PO_3$, etc.) to create strong chemical bonds with the photoanode surface and likely to be as a bridge for electron injection.[8−10] Polypyridyl ruthenium(II) derivatives are one of the most popular and widely used dyes in solar cells. In ruthenium complexes, bipyridine ligands can attach to the surface of semiconductors using carboxylic groups and provide a strong electronic coupling for the excited electron injection process, as well as rapid regeneration of the oxidized dye by thiocyanate ligands.[11,12] In particular, di-tetrabutylammonium *cis*-bis(isothiocyanato)bis(2,2′-bipyridyl-4,4′-dicarboxylato)-ruthenium(II) (N719) has received more attention due to its high chemical stability and rapid electron injection after light absorption.[13]

The electrolyte solution facilitates the process of the charge transfer between the counter and the working electrodes and also regenerates the oxidized dye. Conventional electrolytes in DSSCs are based on the iodide/triiodide redox couple, which are mostly dissolved in an organic solvent such as acetonitrile (ACN), and have shown good efficiencies.[14,15] The type of metal salt (LiI, KI, NaI, etc.) in the electrolyte solution is a key factor. If small cations such as lithium (Li^+) are used, they can be adsorbed on the surface of nanoparticles and have an effect on electrolyte and photoanode interactions.[16,17] By adsorbing small cations on the photoanode surface, the Fermi state and the edge of the conduction band (CB) change in a positive direction, forming a better electronic coupling that speeds up the electron injection from the dye into the semiconductor CB and also improves photocurrent density (J_{sc}).[18,19] On this topic, we can refer to the report of Teo et al., investigating of

Received: May 12, 2021
Revised: July 4, 2021
Accepted: July 7, 2021
Published: July 19, 2021

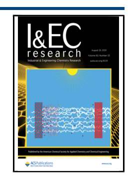

the effect of lithium iodide on the DSSC performance using polymer gel electrolytes.[20]

In previous studies, many semiconductors have been used as photoanodes, such as ZnO,[21] SnO_2,[22] Nb_2O_5,[23] TiO_2,[24] and so forth. Among these materials, TiO_2 had the best efficiency till date; porous structure and appropriate band gap are the factors that make TiO_2 suitable and pointed out that they cause more dye adsorption on the surface and easier electron-transfer process, respectively.[25,26] Among all the proposed metal oxide semiconductors, performance of Bi_2WO_6 nanoparticles in DSSCs has not yet been examined. There are different methods for preparing Bi_2WO_6 nanoparticles that cause differences in their structure; common methods include microwave-assisted,[27] co-precipitation,[28] sol−gel,[29] and hydro-solvothermal methods.[30] Nanoparticles, slit-like, octagonal, microspheres, flower-like structures, nanocoating's, nanoplates, and hollow structures are of various Bi_2WO_6 forms.[31,32] Bi_2WO_6 has important applications, including catalysts, optical fibers, chemical sensors, and magnetic devices.[32] Ferroelectricity, piezoelectricity, high conductivity, and photocatalytic sensitivity are some properties of Bi_2WO_6.[33]

Molecular dynamics (MD) simulation is a theoretical tool utilized to explain how the velocities, positions, and orientations of reciprocating atoms change over time.[34] MD simulations can typically be used to model the time-dependent motions (trajectories) of electrolytes and dyes in a DSSC and give us information on how they interact with solid surfaces. In this regard, the MD investigation of confined ionic liquids between slit-shaped nanosized pores can be mentioned.[35,36]

In the present study, the effect of Bi_2WO_6 nanostructure as photoanode on DSSC functions was investigated. The photoelectrochemical response of Grätzel-type solar cells was determined on the basis of these semiconductors and their sensitivity to dyes. Moreover, in this work, the effect of various parameters, namely, the pH condition during synthesis of this nanostructure, the amount of film thickness, the band gap energy, and the surface charge on the photovoltaic performance of DSSCs were evaluated. The intermolecular interactions of dye solution with Bi_2WO_6 surface were also studied by MD simulation, whereas the relative arrangement of the dye molecules close to the Bi_2WO_6 surface was examined. Our work also provides new insights into interactions between the Bi_2WO_6 surface and electrolyte mixture from surface chemistry view point in order to obtain a relation between their photovoltaic activity and chemical surface. For comparison purpose, the performance of titanium dioxide nanostructures as photoanode in terms of computational and experimental methods was also tested.

2. METHODS

2.1. Materials. Conductive glass plate (FTO glass, fluorine-doped SnO_2, and sheet resistance 15 $\Omega \cdot cm^{-2}$) and platinum paste were purchased from Sharif solar. TiO_2 nanoparticles, ethanol, ethyl cellulose (EC), terpineol, $Bi(NO_3)_3$, $Na_2WO_4 \cdot 4H_2O$, ACN, lithium iodide (LiI), iodine (I_2), and also N719 dye powder were purchased from Sigma-Aldrich (US Research Nanomaterial, Lnc, USA). All materials and reactants were of analytical grade and utilized without further purification.

2.2. Preparation of Photoanodes with Bi_2WO_6 Nanoparticles and TiO_2 Nanoparticles. In this paper, the hydrothermal method was used to synthesize Bi_2WO_6 nanoparticles. 3D flower-like Bi_2WO_6 was grown hydrothermally without any templates. To this aim, 0.73 g of $Bi(NO)_3$ was solvated in 20 mL of deionized (DI) water and stirred at 700 rpm for 30 min. In another vessel, 0.24 g of $Na_2WO_4 \cdot 4H_2O$ was added to the 30 mL of DI water and stirred for 30 min. The solution was added to the first vessel and stirred for 60 min at 40 °C. The white precipitate transferred to 80 mL capacity Teflon-lined stainless-steel autoclave and kept at 160 °C for 16 h. Then, the autoclave was cooled to room temperature. The product was washed and filtered several times by ethanol and DI water, respectively. The white powder was desiccated in an oven for 12 h at 90 °C. Over the three selected pH values (1, 8, and 12), the Bi_2WO_6 nanostructures were synthesized. For adjusting the pH, NaOH solution (0.1 M) was used. The effect of pH on morphologies, surface area, and dye absorption was investigated. For comparison purpose, the TiO_2 nanoparticle photoanode was also constructed. To make different pastes, 0.03 g of EC was added to 2 mL of ethanol in a glass vial at 500 rpm and 60 °C on a magnetic stirrer. After dissolving, 0.5 mL (500 μL) of terpineol was added to the solution using a micropipette and placed it on the magnetic stirrer again for 5 min to mix thoroughly. At this step, 0.03 g of Bi_2WO_6 nanoparticles was completely dispersed in the mentioned solution by using the ultrasonic bath for 30 min. Then, the sonicated mixture was located in the paraffin oil bath at 60 °C for 24 h under intensive stirring until the ethanol completely evaporates and uniform paste forms. The above steps for making pastes of Bi_2WO_6, synthesized under different pH conditions, and also for TiO_2 were performed. We also prepared three various pastes in which ratios of Bi_2WO_6 to TiO_2 were fixed at 25, 50, and 75%. The process of making the mixed Bi_2WO_6/TiO_2 pastes starts with the preparation of the Bi_2WO_6/TiO_2 nanomaterial powder. In this way, the first mixture consisted of 25% Bi_2WO_6 powder + 75% TiO_2 powder, the second mixture consisted of 50% Bi_2WO_6 + 50% TiO_2, and the third is a mixture of 75% Bi_2WO_6 + 25% TiO_2 powder. Thereby, ethanol, EC, and terpineol were added to mixed powders based on the mentioned paste procedure and stirred for 24 h.

2.3. Fabrication of the DSSCs. The FTO substrates with a resistivity conductor of 15 $\Omega \cdot cm^{-2}$ were ultrasonically cleaned in detergent solution, acetone, ethanol, and then rinsed with DI water for 15 min, respectively. After complete washing, we dried all the pieces completely. The printing paste on a FTO was coated using the Doctor Blade method on the freshly cleaned substrates with dimensions of 2 cm × 1.5 cm. The photoanode electrodes were annealed in a furnace at 450 °C for 60 min. The thickness of the photoanode was obtained to be 3.24 μm at this condition [see Figure S1, scanning electron microscopy (SEM) cross-view]. Then, a commercial Pt paste (Sharif solar) in the form of a viscous paste was also coated on the FTO using the Doctor Blade technique. Then, the as-prepared cathode was annealed in the furnace for 30 min at a temperature of 400 °C. To prepare a 0.4 mM solution of N719, 11.885 mg (0.012 g) of N719 was poured into a 25 mL volumetric balloon, and ethanol was added as the solvent. Then, the dye mixture was stirred for 24 h. During the DSSC fabrication times, dye solution was stored away from the light, and for dye-sensitization, the photoanodes were immersed in the dye solution overnight at room temperature in the dark, so that the dye molecules could be well adsorbed on the surface of TiO_2 and Bi_2WO_6. The electrolyte solution was composed of ACN as the solvent, LiI (0.2 M), and iodide I_2 (0.02 M). The electrolyte solution was inserted in the interspace between the two electrodes of the DSSCs, so that it can flow over the

https://doi.org/10.1021/acs.iecr.1c01812
Ind. Eng. Chem. Res. 2021, 60, 12292−12306

surfaces of electrodes, pressing tightly. To avoid short-circuiting between two electrodes, a thin layer of Surlyn was used as a hot-melt spacer. To finalize the assembly of the DSSCs, by using alligator clamps, an electrical connection was established between the counter and working electrodes.

2.4. Instrumentation and Measurements. Solar radiation is not always available, so to measure the efficiency of a solar cell, a solar simulator is mostly used that can have constant and continuous radiation and provides the same environmental conditions for each cell. Herein, photocurrent density−voltage ($J-V$) curves were measured under a solar simulator [AM 1.5 illumination (100 mW cm^{-2})] in combination of an autolab electrochemical system equipped with GPES software.[37]

2.5. Characterization Methods. The prepared Bi_2WO_6 samples were characterized by using powder X-ray diffraction (XRD) analysis to find the crystallinity and phase of the sample using a Cu Kα radiation source (λ = 1.54060 Å) at room temperature in the range of 2θ = 10−80 with a scan rate of 0.1° 2θ s^{-1}. UV−vis diffuse reflectance spectra were performed using a UV−vis diffuse reflectance spectrophotometer (Shimadzu UV-2550) with Ba_2SO_4 pellet as the reference sample. Energy-dispersive X-ray (EDX) spectroscopy was used to evaluate the relative amounts of elements in the samples. The surface morphology and cross-sectional structure of Bi_2WO_6 and TiO_2 nanoparticles and pastes were observed using SEM. Barret−Joyner−Halenda (BJH) and Brunauer−Emmett−Teller (BET) analyses (were computed from the nitrogen adsorption−desorption evaluations at 77 K) were carried out to know the pore volume, surface area, and pore size distribution of the synthesized Bi_2WO_6. To pre-clean the surface of the samples tested, before measurement, all materials were degassed at 100 °C for 2 h under high vacuum. Surface charge of the nanoparticles was determined using zeta potential measurements at room temperature using Milli-Q water as the dispersant. The presence of binding residence and the functional groups of the Bi_2WO_6 were determined by Fourier transform infrared spectroscopy (FTIR) and have been taken in the selection of 400−4000 cm^{-1}. The adsorption of dye on Bi_2WO_6 (which fabricated at different pH) was measured by recording N719 absorption intensity change at maximum wavelengths (527 and 386 nm). The dye solution absorption was measured using a UV spectrophotometer (Shimadzu), as described in following. The N719 dye solution of 50 mg/L was prepared in ethanol solvent. Then, 0.01 g of Bi_2WO_6 nanoparticles at different pH was dipped into a 5 mL adsorption vessel containing 50 mg/L N719 solution and a stirrer rotated at 200 rpm for 30 min. Each sample was withdrawn regularly from the adsorption vessel via micropipette for UV analysis.

2.6. Computational Details. In this work, N719 dye with molecular formula of $C_{58}H_{86}N_8O_8RuS_2$, ethanol, and ACN molecules were optimized by the hybrid density functional method (B3LYP), using Gaussian 09 program,[38] with the LANL2DZ pseudopotential[39] for Ru and 6-31G(d) basis set for O, N, C, S, and H atoms. The computed structures were controlled for vibrational frequencies, ensuring that the state of minimum energies was achieved on the potential energy surface. Besides, new sets of partial charges were assigned by performing population analysis using the natural bond orbital (NBO) method.[40] We also performed the simulations by using the charges from electrostatic potential (ESP) using a grid-based method (ESP-based charges). As no significant differences in structural characteristics of systems due to the atomic charges were noted, we continued the simulations using the NBO charges.

Four different systems were simulated to investigate the ordering and structure of electrolyte solution and dye solution near the solid surfaces. Simulations were carried out with the GROMACS 5.1.5 program.[41] Lennard-Jones (LJ) parameters (σ_i: the distance parameter and ε_i: the parameter expressing the strength of interactions) employed to model ethanol, LiI, ACN, and N719 molecules were obtained from the OPLS-AA parameters. The parameters used to model the intermolecular and intramolecular interactions of the titanium and oxygen atoms in the anatase TiO_2 slabs as LJ spheres were σ_{Ti} = 0.392 nm, ε_{Ti} = 0.041 kcal mol^{-1} and σ_O = 0.303 nm, ε_O = 0.12 kcal mol^{-1}.[42] The atomic charges on the titanium and oxygen of TiO_2 were +2.196e and −1.098e, respectively.[42] In the platinum wall, the platinum atoms were modeled using the following parameters: ε_{Pt} = 7.80 kcal mol^{-1} and σ_{Pt} = 0.285 nm.[43] Also, the parameters used to model the interactions of the bismuth, tungsten, and oxygen atoms in the Bi_2WO_6 walls as LJ spheres were σ_{Bi} = 0.280 nm, ε_{Bi} = 1.729 kcal mol^{-1}, σ_W = 0.340 nm, ε_W = 0.621 kcal mol^{-1}, σ_O = 0.309 nm, and ε_O = 0.14 kcal mol^{-1}.[44,45] The atomic charges on the bismuth, tungsten, and oxygen atoms were +2.470e, +3.70e, and −1.440e, respectively.[46] Accordingly, the positions of the slab atoms were kept frozen during the simulations. Therefore, throughout the simulation times, only the electrolyte and dye solutions were allowed to relax, and the atoms of surfaces have been constrained to maintain in fixed positions.

In line with experimental results, the aim of MD simulations was to compare the TiO_2 and Bi_2WO_6 nanostructures as photoanodes of DSSCs considering the interaction of N719 dye solution and also the electrolyte with these two structures. To evaluate the photoanode performance, we simulated two models: in the first model, the electrolyte solution was located between the walls of anatase TiO_2(101) and platinum. In the second model, the electrolyte was located between the Bi_2WO_6(100) and platinum walls. In this regard, a model system containing 40 ion pairs of LiI in ACN solvents (4000 molecules) was simulated for 20 ns under the isothermal−isobaric (NPT) ensemble condition as the bulk phase of the electrolyte solutions. In the case of solid/liquid interface simulations, the equilibrated bulk ensemble of electrolyte solution was confined inside slit-like nanosized pores (10 nm) comprising TiO_2/Pt or Bi_2WO_6/Pt slabs in the y-direction. Auxiliary walls were located to avoid the diffusion of the electrolyte into the vacuum regions on bottom and top of the slit pores in the y-direction as a graphene layer. The parallel walls of nanopores were made of TiO_2 (4.30 × 0.83 × 5.86 nm)/Pt (4.23 × 0.68 × 6.16 nm) or Bi_2WO_6 (5.58 × 1.24 × 3.68 nm)/Pt (6.12 × 1.08 × 3.78 nm) slabs.

In the other two model simulations, distribution of the N719 dye solution between Bi_2WO_6/Bi_2WO_6 and TiO_2/TiO_2 slabs was investigated. N719 solution containing 60 molecules of N719 dye in ethanol solvent (6000 molecules), as the bulk phase of the mixture, was equilibrated under NPT condition for 20 ns. We did not consider the counterions in these model systems since their effect on the excited-state and ground energy levels has been predicted to be negligible.[11,47] The resulting structures were then utilized to start the MD simulation steps, and initial energy minimizations were conducted, at first. Then, equilibration was conducted by the canonical ensemble (NVT), using the velocity-rescaling

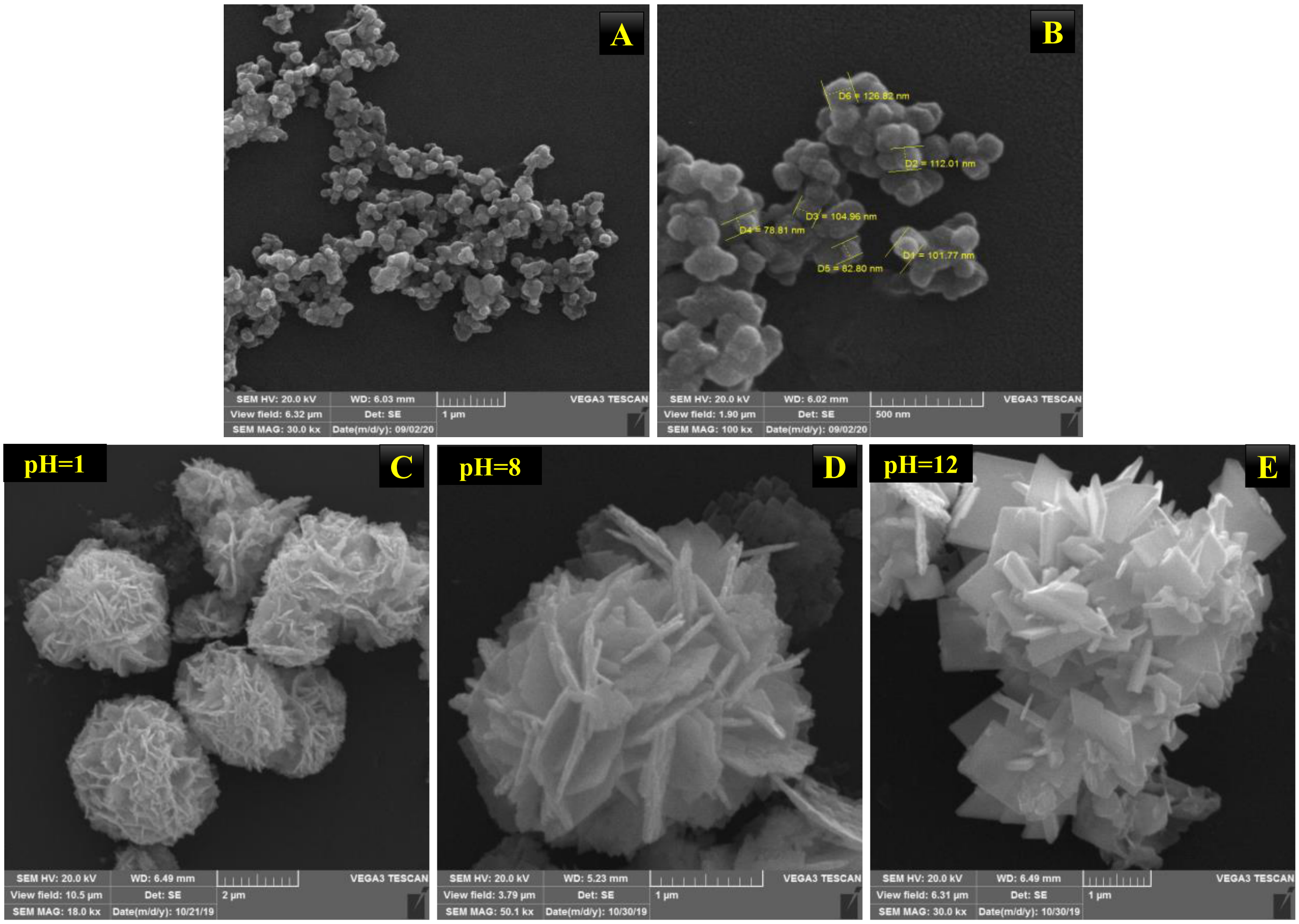

Figure 1. SEM images of TiO_2 (A,B) and Bi_2WO_6 samples obtained at different pH values (C−E).

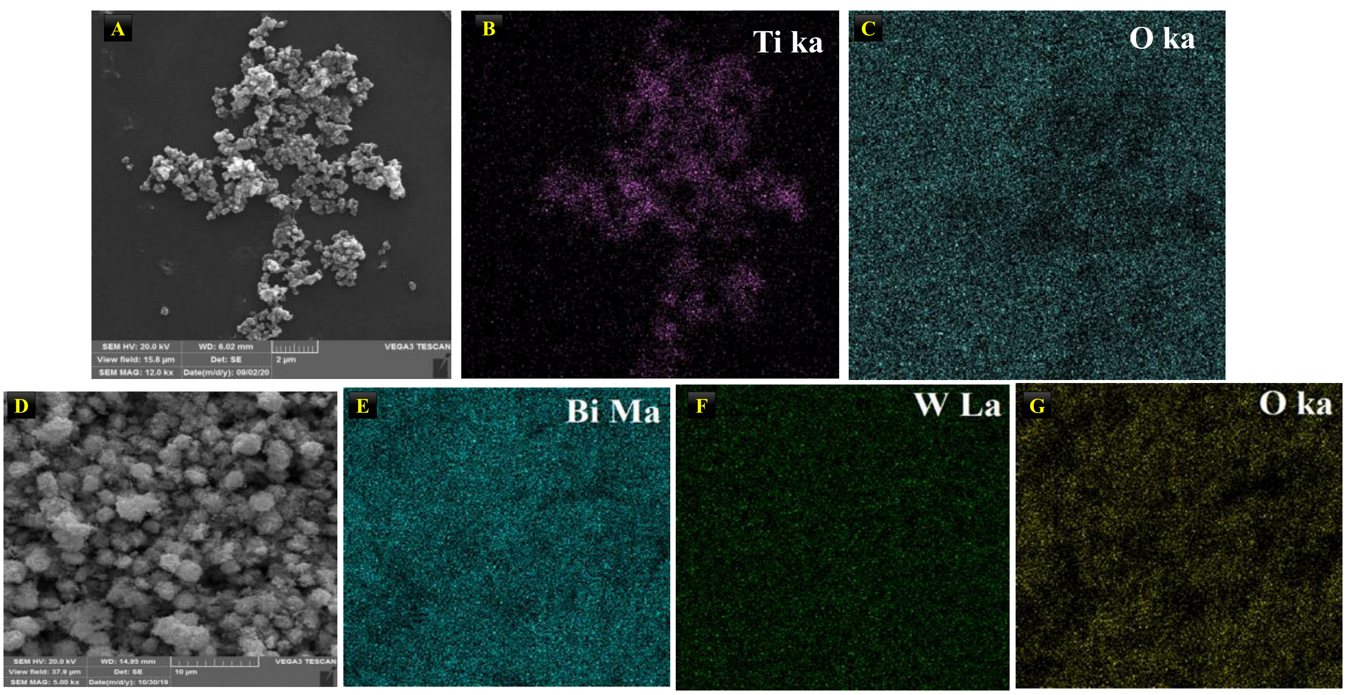

Figure 2. EDX mapping of TiO_2 (A−C) and Bi_2WO_6 (D−G).

thermostat with 0.1 ps time constant to maintain the temperature (300 K) of the system.[48] The final simulation runs were performed for 10 ns at 300 K in the *NVT* ensemble with time steps of 1 fs. For each simulation, the cutoffs for

https://doi.org/10.1021/acs.iecr.1c01812
Ind. Eng. Chem. Res. 2021, 60, 12292−12306

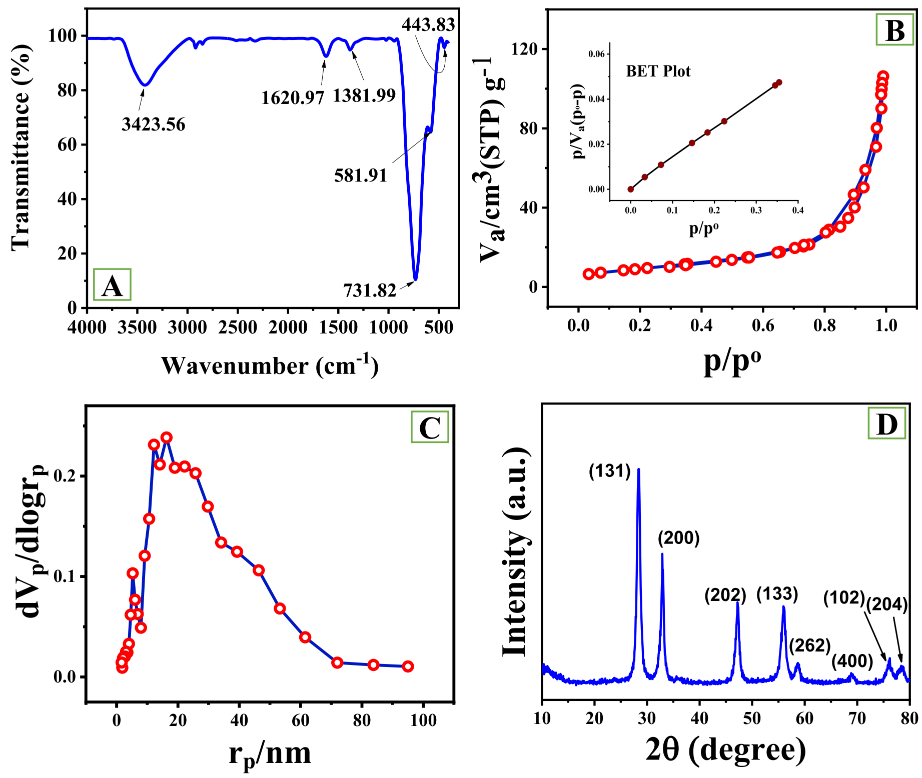

Figure 3. FTIR spectrum of the Bi_2WO_6 structure (A), N_2 adsorption−desorption isotherm (B), BJH plot of Bi_2WO_6 (C), and XRD pattern of Bi_2WO_6 (D).

nonbonding interactions were selected to be 12 Å. The Coulombic long-range interactions were calculated utilizing the particle-mesh Ewald method with a cutoff distance of 15 Å.

3. RESULTS AND DISCUSSION

3.1. Characterization. *3.1.1. Scanning Electron Microscopy/Energy-Dispersive X-ray Spectroscopy.* Figure 1A,B demonstrates the SEM images of the studied TiO_2 nanoparticles with a diameter of 70−130 nm. Figure 1C−E shows typical SEM images of the synthesized products using the hydrothermal method of the Bi_2WO_6 solutions with pH of 1, 8, and 12. The products were composed of 3D flower-like nanostructures. Upon adjusting the pH to higher values, the 3D flower-like Bi_2WO_6 structure grew and agglomerated to form clusters of fully nanoplates. Based on SEM analyses, pH values of the precursor solutions affected the morphologies of the as-synthesized Bi_2WO_6. As shown in Figure 2A−G, the EDX elemental mapping images illustrate the uniform distribution of Ti, O and Bi, W, O in the whole parts of TiO_2 and Bi_2WO_6 structures, respectively.

3.1.2. FTIR Spectrum Analysis. As can be seen in Figure 3A, the absorption bands from 400 to 4000 cm^{-1} could be ascribed to the stretching and bending modes of O−H group on the surface of Bi_2WO_6 samples. The strong sharp bands at 500−1400 cm^{-1} belonged to the W−O stretching, Bi−O stretching, and W−O−W bridging modes.[49] The Bi−O and W−O stretching bands were placed at 581.91 and 731.82 cm^{-1}, respectively, and the W−O−W bending vibration mode was centered at 1381.99 cm^{-1}.[50,51] The absorption bands at 1620 and 3423 cm^{-1} could be attributed to the stretching and bending modes of O−H on the surface of the sample.[52] No characteristic absorption peak was found in the FTIR spectra, which indicated that the as-prepared Bi_2WO_6 samples were all pure.

3.1.3. N_2 Adsorption−Desorption Isotherms. The N_2 adsorption−desorption isotherm of Bi_2WO_6 is depicted in Figure 3B, wherein amount of N_2 adsorbed $[V_a\ (cm^3 \cdot g^{-1})]$ is plotted versus relative equilibrium pressure (P/P^0). P^0 and P are the vapor pressure of the bulk liquid nitrogen and equilibrium pressure of desorption at the liquid nitrogen temperature (∼77 K). The BET surface area and the pore volume for Bi_2WO_6 were obtained to be 32.27 $m^2 \cdot g^{-1}$ and 0.1616 $cm^3 \cdot g^{-1}$, respectively. The BJH model (Figure 3C) was applied for the investigation of porosity which revealed a mean pore diameter of 19.42 nm for Bi_2WO_6 [r_p (nm) is pore radius]. The nanostructures were mesopores, according to the BET classification, and the hysteresis loop for photocatalysts was type III, according to the IUPAC classification.[53−55]

3.1.4. Powdered XRD. XRD was used to evaluate the crystallinity and phase structure of Bi_2WO_6. Figure 3D demonstrates the XRD patterns of Bi_2WO_6 structure. The phase purity of the sample was approved, and diffraction peaks for Bi_2WO_6 were indexed as 2θ = 28.2, 32.7, 47.1, 55.9, 58, 69, 76, and 78°, which are related to the diffraction peaks of the (131), (200), (202), (133), (262), (400), (102), and (204) crystal planes of Bi_2WO_6, respectively (JCPDS no. 39-0256).[56] The crystallinity was high, and no peaks related to impurities were observed. The average crystalline size of nanoparticles can be calculated by Scherrer's equation, $d = 0.9\lambda/\beta \cos\theta$, in which θ, λ, and β are the position of the plane peak, X-ray wavelength, and full width at half-maximum of the peak, respectively.[57] In good agreement with the previous investigations,[58,59] the average crystalline size of the synthesized Bi_2WO_6 was obtained to be 15.3 nm from the broadening of the (131) diffraction peak.

https://doi.org/10.1021/acs.iecr.1c01812
Ind. Eng. Chem. Res. 2021, 60, 12292−12306

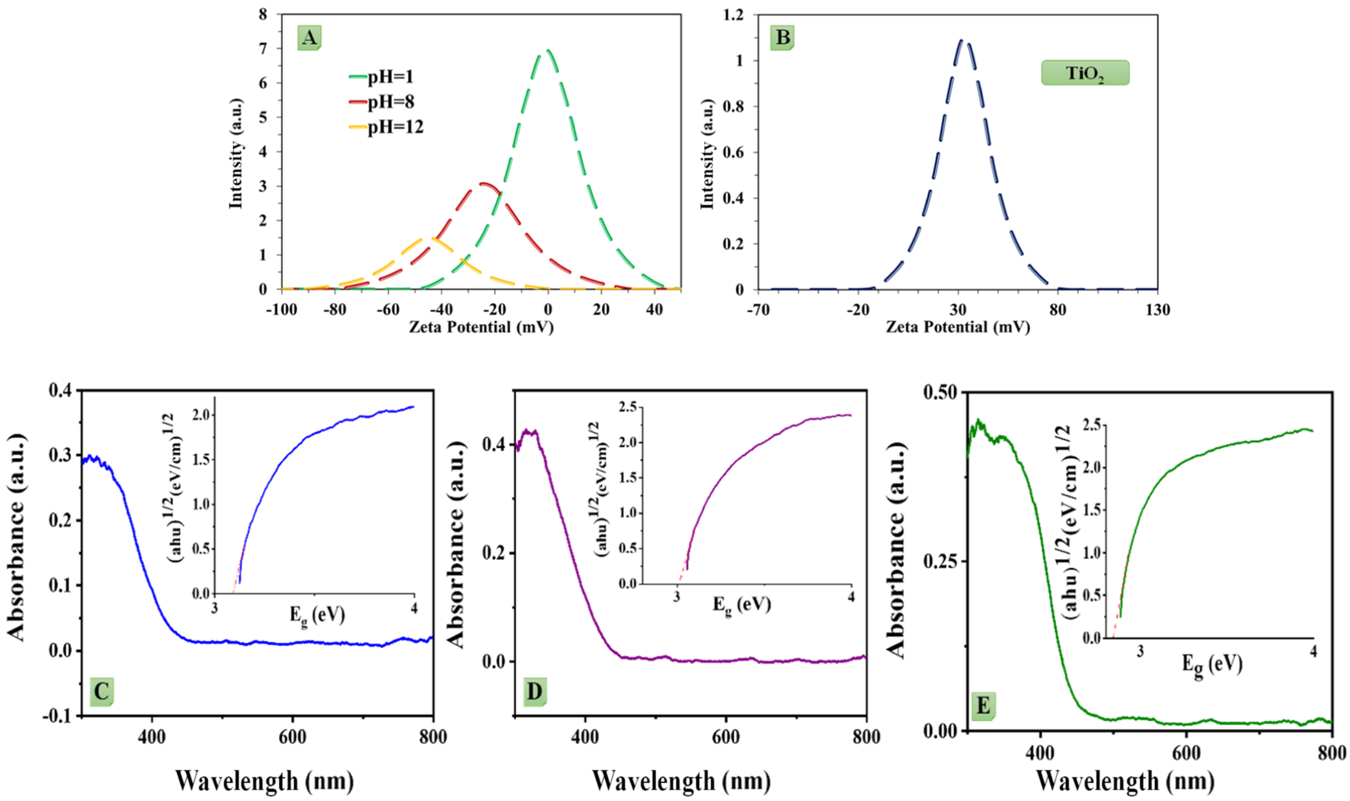

Figure 4. Zeta potential of the Bi_2WO_6 nanoparticle at pH = 1, pH = 8, and pH = 12 (A), zeta potential of the TiO_2 nanoparticle (B), and UV−vis absorption spectrum and energy band gap of the Bi_2WO_6 nanoparticle at pH = 1 (C), pH = 8 (D), and pH = 12 (E).

3.1.5. Zeta Potential Analysis. Zeta potential measurements were used to investigate the surface charge of Bi_2WO_6 and TiO_2 nanoparticles. Bi_2WO_6 and TiO_2 powders were first dispersed in water before measuring the zeta potential. The zeta potential values have been measured for different pH values of Bi_2WO_6 and TiO_2 nanoparticles. As depicted in Figure 4A,B, the zeta potential of pH 1, 8, and 12 of Bi_2WO_6 is in the range of −0.9, −24.2, and −44.9 mV, respectively; and also, the zeta potential is observed to be around 33.2 mV for TiO_2. These results demonstrated that the TiO_2 nanoparticle surface charge is positive completely. The Bi_2WO_6 surface charges turn to higher negative values by increasing the pH.

3.1.6. UV−Vis Diffuse Reflectance Spectroscopy. The energy band gap of the pH values 1, 8, and 12 of the synthesized samples of Bi_2WO_6 was estimated from the UV−vis absorption spectrum using the Tauc/David-Matt model (eq 1).[60]

$$(\alpha \cdot h\nu)^{1/n} = A(h\nu - E_g) \quad (1)$$

where α, h, ν, A, and E_g are absorption coefficient, the planck's constant, photon's frequency, a constant, and band gap energy, respectively. The absorption of continuous light for three different pH values of Bi_2WO_6 was observed in the range of 400−700 nm, which determined the light absorption of these three pH conditions. Figure 4C−E shows that by increasing the pH from 1 to 12, the band gap value becomes smaller, and for pH of 1, 8, and 12, this value is equal to 3.24, 3.07, and 2.81 eV, respectively. As a result, pH = 1 shows the largest band gap, and therefore, the Bi_2WO_6 CB was closer to the dye's lowest unoccupied molecular orbital (LUMO) energy level at this pH, which allows the electron injection process to occur better and faster.[61,62] Therefore, pH = 1 can be expected to perform better in the electron-transfer process from the dye LUMO to the Bi_2WO_6 CB in the DSSC. To provide the proof of concept, the CB and valence band (VB) edge position of Bi_2WO_6 at pH = 1, pH = 8, and pH = 12 were determined by the following empirical formulas[63]

$$E_{VB} = X - E_e + 0.5E_g \quad (2)$$

$$E_{CB} = E_{VB} - E_g \quad (3)$$

$$X = [X(A)^a X(B)^b]^{1/(a+b)} \quad (4)$$

wherein E_{CB} and E_{VB} are CB and VB potential of semiconductor, respectively, and X is the electronegativity of the photocatalyst. $X(i)$ is electronegativity of the constituent atoms (A and B), and a and b are the number of those atoms. X value for Bi_2WO_6 is 6.363 eV.[55] E_e is the free-electron energy [on the hydrogen scale (∼4.5 eV)],[64] and E_g is the band gap energy. E_{VB} for Bi_2WO_6 at pH = 1, 8, and 12 was calculated to be 3.48, 3.39, and 3.27 eV, and E_{CB} for Bi_2WO_6 at these pH conditions was 0.24, 0.32, and 0.46 eV, respectively (see Scheme 1).

3.1.7. Absorption Spectra Properties. The UV−vis absorption spectra of the N719 sample in ethanol solution revealed two broad bands, as shown in Figure 5. The two broad visible bands at 527 and 386 nm were assigned to metal-to-ligand charge-transfer origin. Optical absorption spectra of the N719 dye solution in the presence of Bi_2WO_6 nanoparticles with different pH conditions are also compared in the Figure 5. Bi_2WO_6 at pH = 1 has significantly affected the absorption peaks of N719. As illustrated and based on the zeta potential results, the less negative surface charge of Bi_2WO_6 at pH = 1 enhanced the adsorption.

https://doi.org/10.1021/acs.iecr.1c01812
Ind. Eng. Chem. Res. 2021, 60, 12292−12306

Scheme 1. Schematic of Band Gap Energies of Bi_2WO_6 at pH = 1, pH = 8, and pH = 12

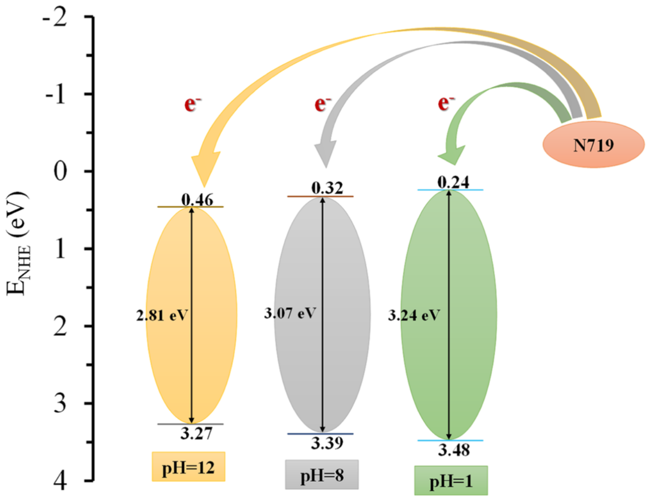

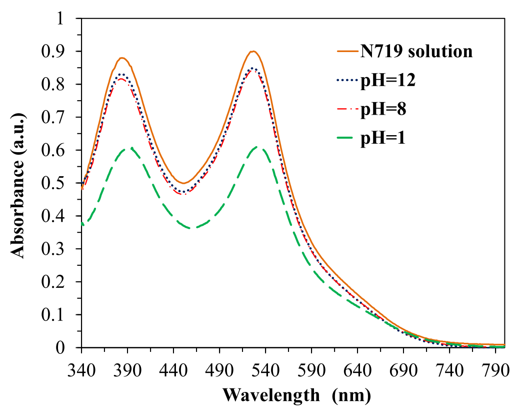

Figure 5. Absorption spectra of N719 dye in ethanol solution and adsorbed onto Bi_2WO_6 nanoparticles with different pH values.

3.2. Photovoltaic Performance of the DSSCs. We conducted synthesis of Bi_2WO_6 nanoparticle powders under different pH values and for comparison purpose, the performance of TiO_2 nanostructures was also tested. The performance and efficiency of fabricated DSSCs based on these nanoparticles were probed by $J-V$ measurements using a sun simulator. Herein, the photovoltaic performance of DSSCs based on Bi_2WO_6 photoanodes prepared in 1, 8, and 12 pH values was evaluated. The various solar cell parameters are collected in Table 1. As shown in Table 1 and also Figure 6A,

Table 1. Photovoltaic Parameters of the DSSCs Based on Bi_2WO_6 Nanoparticles at Different pH Values

composition (Bi_2WO_6)	J_{sc} (mA/cm^2)	V_{oc} (V)	FF	η (%)
pH = 1	0.84	0.65	0.40	0.21
pH = 8	0.54	0.60	0.40	0.13
pH = 12	0.29	0.56	0.35	0.06

the open-circuit voltage decreased when pH increased. A decrease in the short-circuit current was also observed in the case of pH values from 0.84 mA cm^{-2} for pH = 1 to 0.29 mA cm^{-2} for pH = 12. As expected, fill factor (FF) and efficiency of the DSSC based on pH = 1 was higher than pH = 8 and 12. The better performance of DSSC at pH = 1 can be attributed to the high-quality Bi_2WO_6 nanostructures obtained in this pH condition. In fact, the synthesized Bi_2WO_6 nanoparticles were composed of porosity that helped the adsorption of dye, and therefore, more photons can be captured. The surface charge of Bi_2WO_6 (obtained at pH = 1) further increased the performance of the DSSC by enhancing the adsorption of anionic N719 dye. As shown in Figure 6B, by increasing the pH from 1 to 12, the efficiency decreased in the solar cells based on Bi_2WO_6 nanoparticles.

Based on previous observations by Yi-Ming and co-workers, the effect of sintering temperature (160−600 °C) on the physical properties of flower-like Bi_2WO_6 nanoparticles has been investigated.[58] At 160 °C temperature, the surface area and the total pore volume of Bi_2WO_6 have been shown to be the highest. By considering these evidences, we synthesized the Bi_2WO_6 nanostructures at this temperature that helps in better dye adsorption. In order to optimize the DSSCs based on Bi_2WO_6 photoanodes, we examined a new set of experiments to modify the anode pastes using different weights of EC (0.02−0.04 g) as a binder/dispersant.[65] Also, we studied the impact of film thickness on the performance of DSSCs.[66−68] The influence of the film thickness was investigated, and corresponding results are shown in Figure 6C and Table 2. With increasing layer thickness, J_{sc} of DSSCs decreased, and the best performance was obtained for DSSC with 3.24 μm thickness. The effect of EC on DSSCs performances can be seen in Table 3 and Figure 6D. As illustrated, the optimum value of 0.03 g of EC showed the best performance with 0.21% efficiency.

This is the first attempt to investigate the effect of the pH value used in the synthesis of the Bi_2WO_6 on the photovoltaic performance of the corresponding photoanode in DSSCs. In this way, the DSSC assembly conditions were successfully improved, and superior photovoltaic performance is clearly observed for the Bi_2WO_6 at pH = 1 with less negative surface charge. We also examined mixed metal oxides of Bi_2WO_6 and TiO_2, to improve the cell performance by applying TiO_2 nanoparticles with positive surface charge and enhancing the dye adsorption. The comparison between $J-V$ characteristics of DSSCs fabricated with pure Bi_2WO_6 (100% Bi_2WO_6 at pH = 1) and various mixtures with TiO_2 is shown in Table 4 and Figure 7A. In the case of the electrode fabricated at a 25:75 ratio of Bi_2WO_6/TiO_2, mixed powder, J_{sc} of 3.08 mA, solar energy conversion efficiency (η) of 0.88, and FF of 0.46 were obtained. These results were considerably improved in comparison to those resulted from the DSSC with an electrode fabricated by pure Bi_2WO_6 (J_{sc} = 0.84 mA cm^{-2}, FF = 0.40, and η = 0.21, as listed in Table 1). In the case of pure TiO_2 system, the best performance (an overall efficiency of almost 1.36%) was obtained. However, this observation for TiO_2 was quite low due to the effect of large nanoparticles size (70−130 nm), as shown in SEM images of Figure 1B, compared to the previous studies (using nanoparticles with 10−20 nm size in most conventional DSSCs).[69−71] As expected, in Figure 7B, by increasing the percentage of TiO_2 in the $TiO_2-Bi_2WO_6$ mixture, the cell efficiency has been significantly increased.

3.3. MD Simulation Results. *3.3.1. Investigation of Structural and Dynamical Properties of Electrolyte Solution.* Density profiles were examined to determine averaged orientation ordering and spatial positioning of the molecules at the solid/liquid interface. An instant illustration of the distribution of the electrolyte molecules in the electrolyte mixture was calculated by the density profiles across the slabs.

https://doi.org/10.1021/acs.iecr.1c01812
Ind. Eng. Chem. Res. 2021, 60, 12292−12306

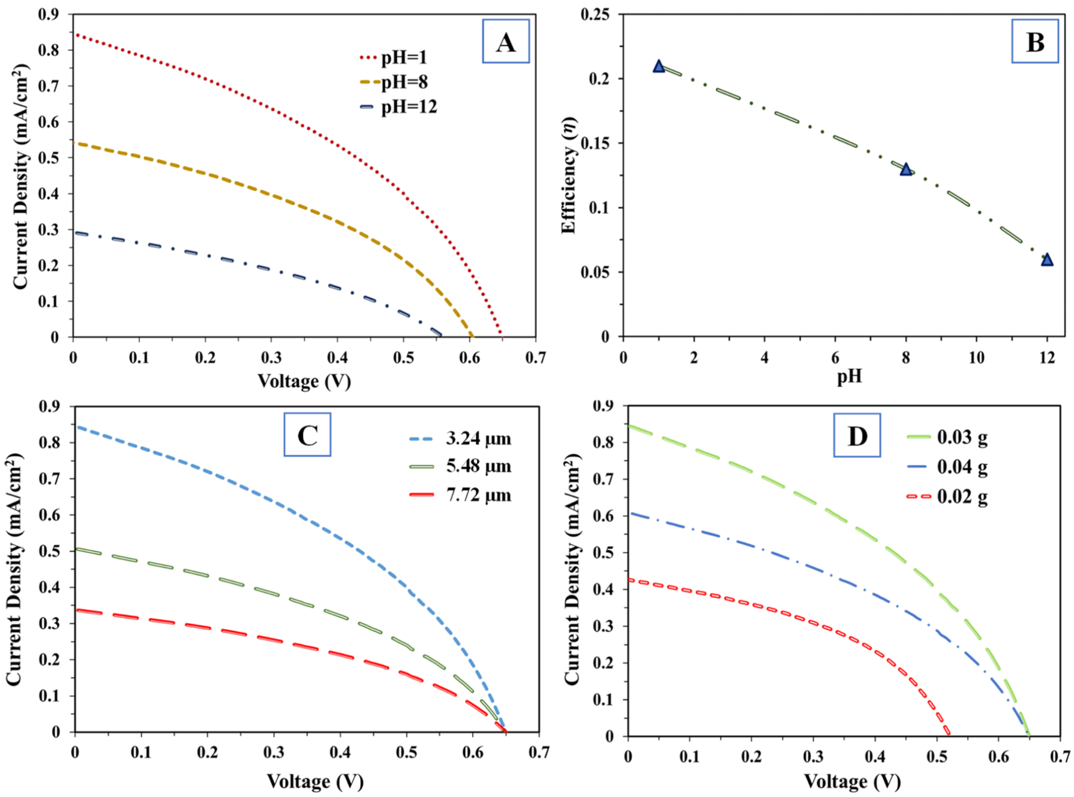

Figure 6. $J-V$ curves of DSSCs using Bi_2WO_6 powder synthesized at pH = 1, 8, and 12 (A) and efficiency of the solar cell vs pH of Bi_2WO_6 (B). $J-V$ curves of Bi_2WO_6 with pH = 1 with different (C) film thicknesses and (D) EC contents.

Table 2. Photovoltaic Parameters of the DSSCs Based on Bi_2WO_6 Nanoparticles with Different Film Thicknesses

composition	thickness (μm)	J_{sc} (mA/cm^2)	V_{oc} (V)	FF	η (%)
Bi_2WO_6	3.24	0.84	0.65	0.40	0.21
	5.48	0.51	0.65	0.39	0.13
	7.72	0.34	0.64	0.38	0.09

Table 3. Photovoltaic Parameters of the DSSCs Based on Bi_2WO_6 Nanoparticles with Different EC Weights

composition	EC content (g)	J_{sc} (mA/cm^2)	V_{oc} (V)	FF	η (%)
Bi_2WO_6	0.02	0.42	0.52	0.42	0.09
	0.03	0.84	0.65	0.40	0.21
	0.04	0.61	0.65	0.33	0.13

Table 4. Photovoltaic Parameters of the DSSCs Based on Bi_2WO_6 and TiO_2 Nanoparticles

composition	J_{sc} (mA/cm^2)	V_{oc} (V)	FF	η (%)
Bi_2WO_6	0.84	0.65	0.40	0.21
75% Bi_2WO_6	1.22	0.68	0.42	0.34
50% Bi_2WO_6	2.01	0.64	0.54	0.69
25% Bi_2WO_6	3.08	0.63	0.46	0.88
TiO_2	4.23	0.62	0.51	1.36

Figure 8A,B exhibits the number density profiles of electrolyte boxes provided by all-atom simulation calculated along TiO_2/Pt and Bi_2WO_6/Pt in the y-direction. The obtained number density profiles demonstrated that for systems, related to the electrolyte solution distribution between solid surfaces, three regions can be identified based on their positions along the y-axis for TiO_2/Pt- and for Bi_2WO_6/Pt-simulated systems: (1) the photoanode/electrolyte solution interface, (2) the Pt/electrolyte solution interface, and (3) the bulk domain (region between 1 and 2).

In the first region (3.5 nm < y < 6.5 nm) for the Bi_2WO_6/Pt model, the number density of the lithium has a considerable peak, while in the region (2 nm < y < 4.5 nm) for the TiO_2/Pt model, the number density of lithium and iodide has strong peaks. In comparison, the density of iodide ions was only on the surface of TiO_2, while on the surface of Bi_2WO_6, only lithium ions can be seen. In the second region of both models, probability density of Li^+ and I^- ions around the Pt surface is substantial. In both models, the number density of ACN is almost the same, and they have the same peaks in the first and second regions. From the number density profiles and MD simulation snapshots of the two models (see in Figure 8), we conclude that the TiO_2 surface has a greater ability to interact with ions, especially iodide ions, than Bi_2WO_6. In particular, a significant influence of the surface structure on the density distribution of I^- at the interface was found. In fact, iodide displays a marked concentration peak at the TiO_2 surface that favored dye regeneration.

The radial distribution function (RDF) in a system of particles describes the probability of finding an atom at a certain distance from a reference atom, according to the statistical averaged over the simulation trajectory. Another method of probing the partitioning of the electrolyte is by computing the RDFs of the electrolyte between the slabs. The RDFs between the anion and cation atoms (Li and I) and ACN atoms (C1, C2, N, and HC) (see the atom labeling of Scheme 2) are displayed and compared in Figure 9. Based on the g(r) plots, the initial strong peak is related to the interaction of Li⋯HC, which is at a distance of 0.17 nm for

https://doi.org/10.1021/acs.iecr.1c01812
Ind. Eng. Chem. Res. 2021, 60, 12292−12306

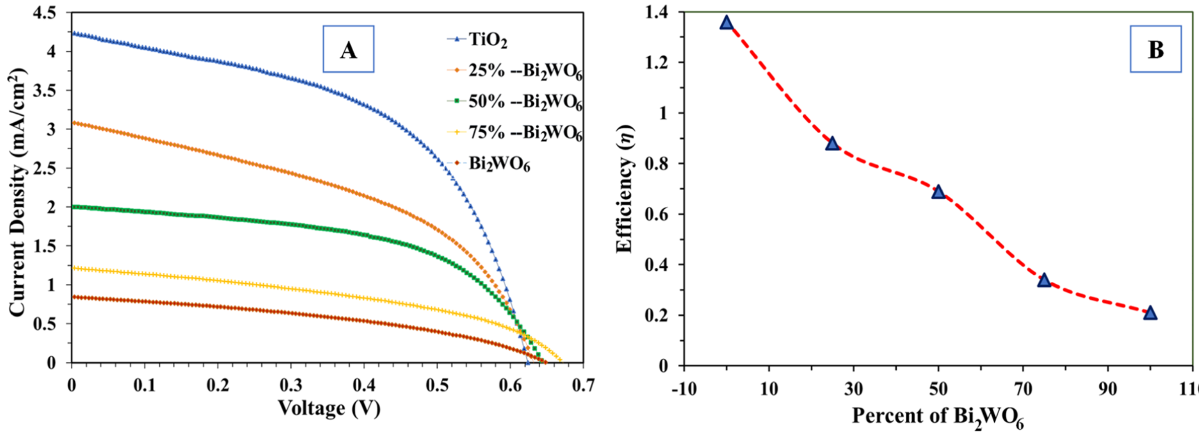

Figure 7. *J*−*V* curves of DSSCs fabricated using Bi_2WO_6 and TiO_2 as photoelectrodes (A) and efficiency of the solar cell vs percent of Bi_2WO_6 (B).

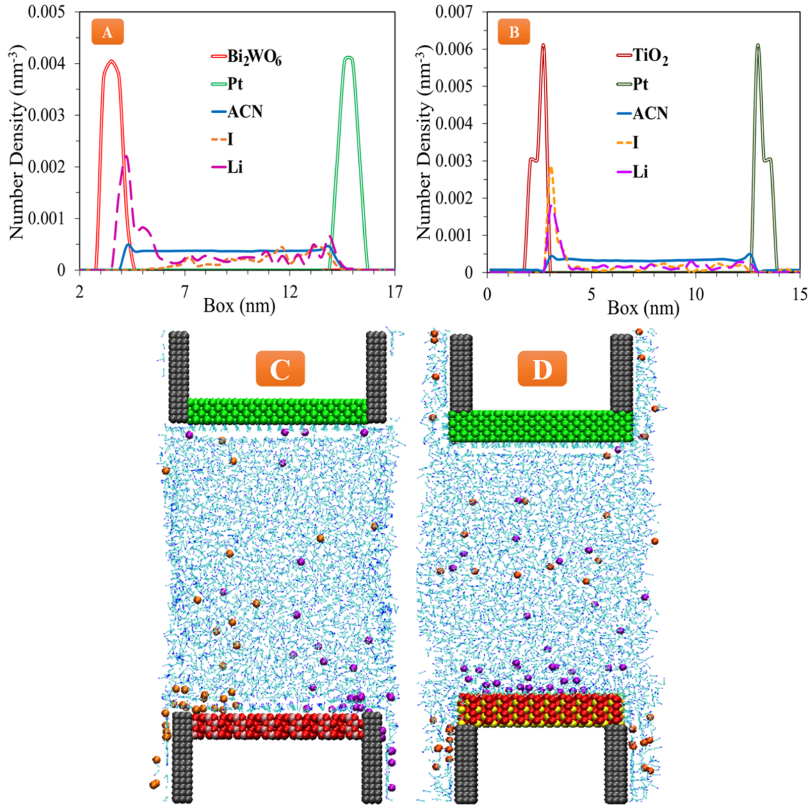

Figure 8. Electrolyte solution's number density profiles of confined inside nanopores of model (A) Bi_2WO_6/Pt and (B) TiO_2/Pt at 300 K and MD simulation sample snapshots of (C) TiO_2/Pt and (D) Bi_2WO_6/Pt models. Lithium and iodide are depicted in violet and orange spheres. Bi, Ti, W, C, O, and N are depicted in yellow, pink, lime, cyan, red, and blue spheres, respectively. Pt atoms are depicted in dark green spheres. ACN molecules are plotted as light blue sticks.

TiO_2/Pt and bulk systems and also at a distance of 0.16 nm for the Bi_2WO_6/Pt system, which represent a strong coordination of lithium ions by ACN molecules. While in the case of I...HC interactions, the location of the first peak in Bi_2WO_6/Pt, TiO_2/Pt, and bulk electrolyte systems is shown to be at distances of 0.32, 0.36, and 0.35 nm, respectively. A strong peak from the interaction of Li⋯C2 is observed, which is located at a distance of 0.25 nm for all systems, while a weaker interaction of I with C2 atoms of ACN is obtained, at a distance of 0.42, see Table S1 for more comparison.

The RDFs between the electrolyte atoms (Li, I, C2, and HC) and solid surface atoms (O and W) (see the atom labeling of Scheme 2) are represented in Figure 9D,E. Four peaks are illustrated for Li⋯O, HC...W (or O), C2⋯W (or O), and I⋯O interactions based on their positions. The distances between atom sites, Li⋯O, HC⋯W (or O), C2⋯W (or O), and I⋯O, are 0.18, 0.23, 0.32, and 0.62 nm, for the Bi_2WO_6/Pt system and 0.25, 0.29, 0.31, and 0.38 nm for the TiO_2/Pt system, respectively. According to the observations, the iodide distance with Bi_2WO_6 is about 0.62 nm in the Bi_2WO_6/Pt system, which is a result of the weak interaction between the I^- and Bi_2WO_6 surface, as previously obtained by number density profiles. The RDF plots disclose that while the Li^+ cations show relatively higher interactions with the Bi_2WO_6 surface, the I^-anions illustrate substantial correlations with the TiO_2 surface.

https://doi.org/10.1021/acs.iecr.1c01812
Ind. Eng. Chem. Res. 2021, 60, 12292−12306

Scheme 2. Structure of ACN, Ethanol, and N719 Dye with Atom Labeling

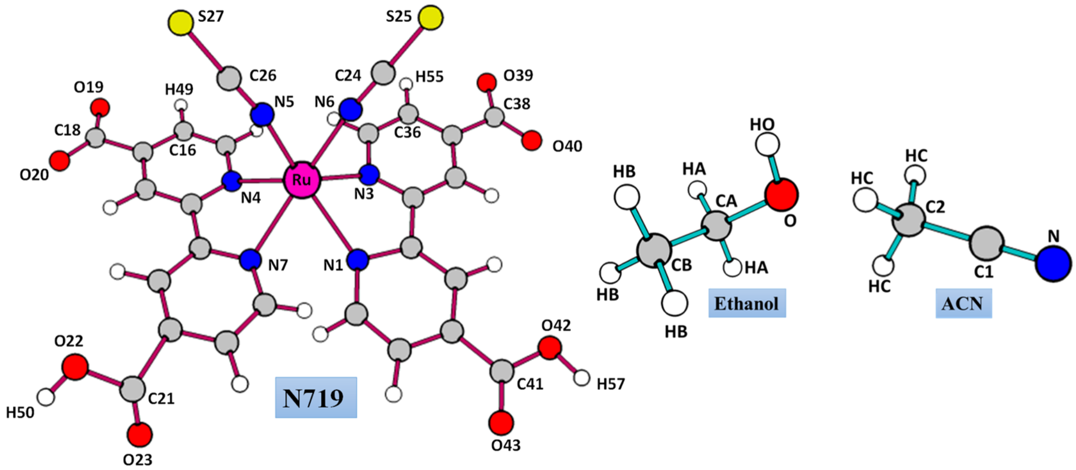

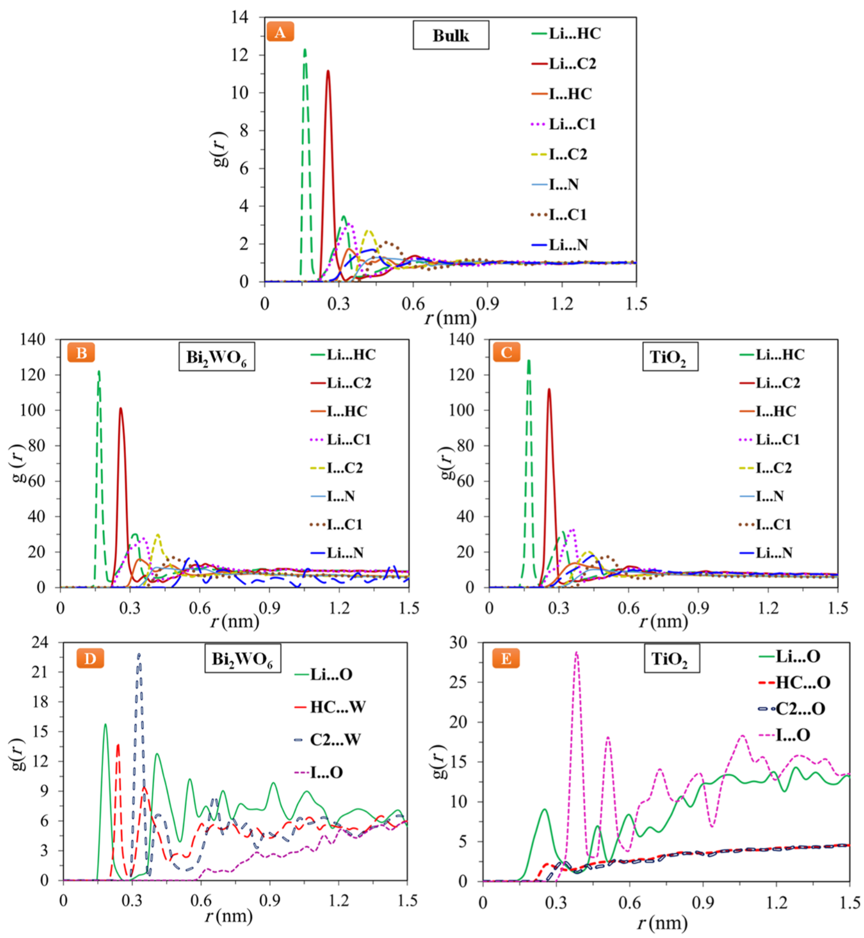

Figure 9. RDFs of Li and I ions with ACN atoms in the bulk system (A), Bi_2WO_6/Pt model (B), TiO_2/Pt model (C), and RDFs of electrolyte atoms (Li, I, HC, and C2) and surface atoms (O and W) in the Bi_2WO_6/Pt model (D) and with the TiO_2/Pt model (E) (see the atom labeling of Scheme 2).

As can be seen in Figure S2, we examined the RDFs between the electrolyte atoms (Li, I, N, C1, C2, and HC) and platinum atom (see the atom labeling of Scheme 2). A comparison of all interactions with platinum is also listed in Table S1. The initial peak is placed at 0.14 nm in the case of Li···Pt interactions in the Bi_2WO_6/Pt model, but in the TiO_2/Pt model, the position of this interaction is about 0.34 nm. Strong and sharp interactions of N···Pt at short distances (0.21 nm) in both models are observed, also the interaction of HC···Pt is located at 0.21 nm in two models.

The transport properties of the confined electrolyte solution were investigated within the framework of mean-squared displacements (MSDs) and are shown in Figure S3. Generally, the MSD is identified as the average distance squared which a particle has moved (away from its starting point) during the

https://doi.org/10.1021/acs.iecr.1c01812
Ind. Eng. Chem. Res. 2021, 60, 12292−12306

time interval τ. Thus, this analysis was obtained from the simulated trajectories

$$\mathrm{MSD}(\tau) = \frac{1}{N}\sum_{i=1}^{N}\langle|\vec{r}_i^{\,c}(t+\tau) - \vec{r}_i^{\,c}(t)|^2\rangle_t \quad (5)$$

where $\vec{r}_i^{\,c}(t)$ is defined as the location of the center of mass of ith particle at time t. An ensemble average over time origins is illustrated by the angular brackets. The component of MSD parallel to the $\vec{a}$ vector, specified in the xz-plane (parallel to the Bi_2WO_6 and TiO_2 slabs), was examined based on the following equation

$$\mathrm{MSD}_{\vec{a}}(\tau) = \frac{1}{N}\sum_{i=1}^{N}\left\langle\left|(\vec{r}_i^{\,c}(t+\tau) - \vec{r}_i^{\,c}(t))\cdot\frac{\vec{a}(t)}{|\vec{a}(t)|}\right|^2\right\rangle_t \quad (6)$$

The slope of the linear domain of the MSD curves from simulation trajectories represents diffusion coefficients of the molecules, D_i, and consequently the dynamics of the system. Related to the Einstein relation, D_i was determined from of the MSD plots

$$D_i = \frac{1}{6}\lim_{\tau\to\infty}\frac{\mathrm{d}}{\mathrm{d}t}\langle|\vec{r}_i^{\,c}(t+\tau) - \vec{r}_i^{\,c}(t)|^2\rangle_{t,i} \quad (7)$$

For the purpose of dynamic determination of the lithium, iodide, and ACN molecules in electrolyte mixtures, the MSD curves were collected over last 10 ns of the MD trajectories for all models. As shown in Figure S3, the simulated MSD of ACN molecules is generally higher than that for the electrolyte ions in both models. As expected, the dynamics of iodide and lithium ions in the bulk solution is found to be more than Bi_2WO_6/Pt and TiO_2/Pt models. In general, the dynamic of ACN molecules in confined and bulk systems are found to be greater than ions. Noticeably, due to the interactions between ions and solid surfaces, the dynamics of ions is decreased when electrolyte solution confined between solid surfaces.

As listed in Table 5, ACN in the bulk has a diffusion coefficient of 23.47 × 10^{-10} $m^2 \cdot s^{-1}$, while when it is placed between solid surfaces, its diffusion coefficient increases, which is equal to 130.33 × 10^{-10} and 79.80 × 10^{-10} $m^2 \cdot s^{-1}$ in the Bi_2WO_6/Pt and TiO_2/Pt systems (by considering the linear part of the MSD, during 2−8 ns time range). In the TiO_2/Pt system, based on RDF plots of Figure 9D,E, iodide has more interaction with the surface; therefore, its diffusion coefficient is reduced compared to the Bi_2WO_6/Pt system. The interaction of lithium with the surface of Bi_2WO_6 is higher; therefore, its diffusion coefficient is lower than that of lithium in the TiO_2 system (see Figure S3 and Table 5).

Table 5. Diffusion Coefficients ⟨D⟩ (10^{-10} $m^2 \cdot s^{-1}$) of Electrolyte Components Obtained from the MSD-Time Curves in the *NVT* Ensemble

system	ACN	Li^+	I^-
bulk (electrolyte solution)	23.47	13.21	15.61
Bi_2WO_6/Pt	130.33	1.96	10.82
TiO_2/Pt	79.80	3.41	4.82

3.3.2. Investigation of Structural and Dynamical Properties of N719 Dye Solution. In order to better clarify the difference of Bi_2WO_6 and TiO_2 photoanodes, the interactions of N719 dye solution with these surfaces will be discussed in the following. To provide the proof of concept, the number density profiles and MD simulation snapshots are illustrated in Figure 10. As can be seen, in the TiO_2 model, the number density of the N719 dye has a considerable peak in the vicinity of TiO_2 surfaces, which demonstrate that dye molecules are aggregated close to the TiO_2 surface. In the Bi_2WO_6 model, while the ethanol form an approximately high density distribution in the vicinity of the Bi_2WO_6 surface, the N719 anions are placed in the second layer after a tightly bound ethanol layer. This difference in the dye adsorption of TiO_2 and Bi_2WO_6 surfaces is also shown in MD simulation snapshots of Figure 10C,D.

The RDF between oxygen atom of ethanol (HO) and N719 atoms (O20, O40, O43, O23, S27, and S25) (see the atom labeling of Scheme 2) is illustrated in Figure 11A−C and Table S2. The placement of three strong interactions of HO···O20, HO···O40, and HO···O23 in bulk is equal to 0.26, 0.26, and 0.28 nm, respectively. The RDF plots of all these interactions in the Bi_2WO_6 system are located at a distance of 0.25 nm. In the case of the TiO_2 system, the interaction of HO···O40 occurred about 0.23 nm. The RDF between hydrogen atoms of N719 dye (H50, H57, H49, and H55) and oxygen atom of ethanol (see the atom labeling of Scheme 2) is also presented in Figure 11D−F, and the location of the peaks is listed in Table S2. In this study, we see that H50 and H57 have strong interactions (located at 0.16 nm) with ethanol oxygen, while weaker interactions of H49 and H55 are also observed at a distance of about 0.25 nm.

The RDF between hydrogen atoms of N719 dye (H50, H57, H49, and H55) and oxygen atoms of Bi_2WO_6 and TiO_2 (see the atom labeling of Scheme 2) is compared in Figure 12A,B. We see that in the Bi_2WO_6 model, the interactions of H55···O and H49···O are located at the distances of 0.25 and 0.27 nm, respectively, while the interactions of H50···O and H57···O are placed at the distances of 0.80 nm and 0.82 nm. The interactions of H57···O, H49···O, H55···O, and H50···O are located at the distance of 0.23, 0.28, 0.35, and 0.36 nm in the TiO_2 system, respectively. It can be concluded that the hydrogen bonds between N719 and the TiO_2 surface were originated from both C−H···O and O−H···O (C16−H49···O, C36−H55···O, O42−H57···O, and O22−H50···O), while in the Bi_2WO_6 system, it was only from C−H···O interactions (C16−H49···O and C36−H55···O).

The RDF between O20, O40, O43, S25, and S27 atoms of N719 and Ti (or Bi) atoms of TiO_2 (Bi_2WO_6) (see the atom labeling of Scheme 2) is elucidated in Figure 12C,D. The interactions of O20···Bi(or Ti), O40···Bi(or Ti), and O43···Bi(or Ti) are located at a distance of 0.27, 0.27, and 0.57 nm in the Bi_2WO_6 and 0.32, 0.25, and 0.30 nm in the TiO_2 system, respectively. Based on the RDFs shown in Figure 12D, a stronger probability of observing O43 atoms at a specified distance of 0.30 nm to the surface of TiO_2 is shown for the TiO_2 system, which is a sign of stronger interactions from the carboxylic acid groups of the dye molecule with the TiO_2 surface than the Bi_2WO_6. We also examined the S···Bi RDFs (see Table S2) and found significant peaks in the RDFs at short distances (0.31 nm for S25 atoms and 0.32 nm for S27 from the NCS ligands).

However, structural data are significant regarding the arrangements in the dye solution, dynamical properties help examine the accessibility and mobility. To characterize the dynamics of the N719 molecules in the ethanol solution, we determined the MSDs for all N719 particles as a function of

https://doi.org/10.1021/acs.iecr.1c01812
Ind. Eng. Chem. Res. 2021, 60, 12292−12306

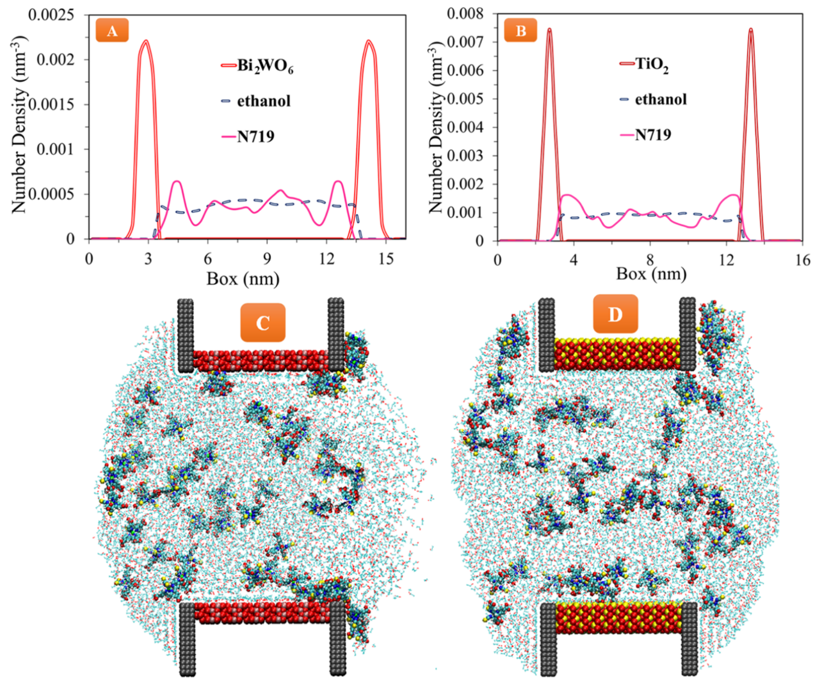

Figure 10. Number density profiles of the dye solutions confined inside nanopores (A) Bi_2WO_6 and (B) TiO_2 in the *y*-direction at 300 K. MD simulation sample snapshots of N719 solution after 10 ns of simulation, (C) TiO_2 and (D) Bi_2WO_6. Ruthenium and sulfur are depicted in purple and dark yellow spheres. Bi, Ti, W, C, O, and N are depicted in yellow, pink, lime, cyan, red, and blue spheres, respectively. O, C, and H atoms of ethanol are shown as red, blue, and white sticks, respectively.

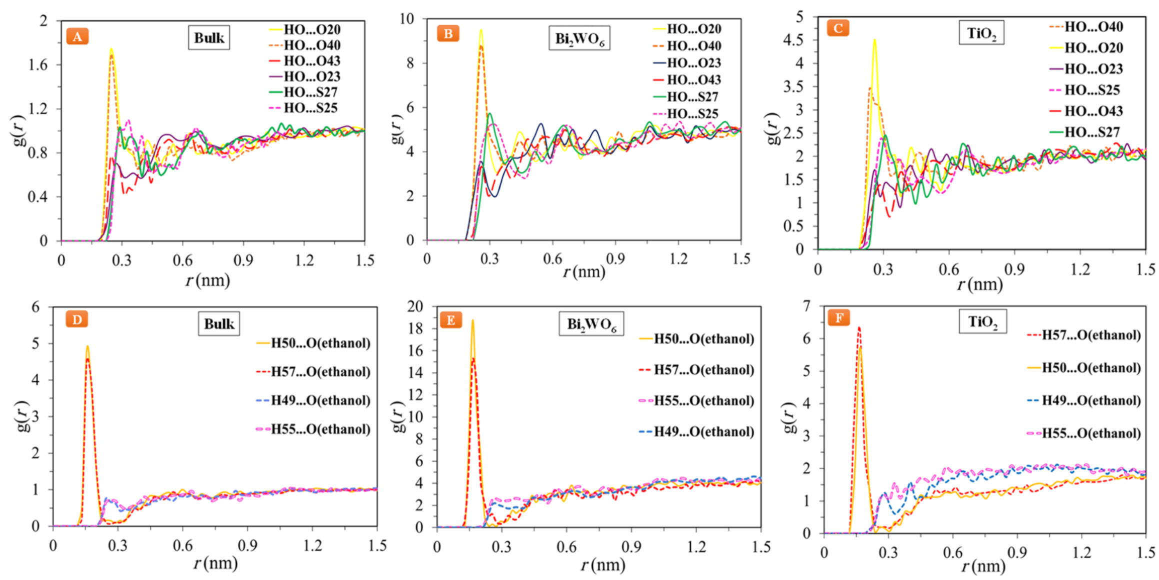

Figure 11. RDFs of hydrogen atoms of ethanol (HO) with N719 atoms in bulk (A),Bi_2WO_6 system (B), and TiO_2 system (C). RDFs of N719··· ethanol interactions in bulk (D), Bi_2WO_6 system (E), and TiO_2 system (F) (see the atom labeling of Scheme 2).

time (see Figure S4). Furthermore, the related simulated diffusion coefficients were calculated and are listed in Table 6. By observing and comparing MSDs for a long time, it is clear that the dynamics of N719 molecules is generally less than that in ethanol molecules. The diffusion coefficient of ethanol in the bulk was obtained to be lower than when located between solid surfaces. In the system of TiO_2, diffusion of ethanol solvent is lower than the Bi_2WO_6 system. The diffusion coefficient of the N719 dye between TiO_2 slabs is also listed to be lower than that between Bi_2WO_6 slabs (see Table 6), indicating that the adsorption of dye on TiO_2 is higher than that on the Bi_2WO_6.

4. CONCLUSIONS

Nanostructures of Bi_2WO_6 particles were successfully fabricated for photoanodes of DSSCs using a simple hydrothermal method. Three types of Bi_2WO_6 photoanodes were fabricated at different pH values, and their performance in DSSCs was evaluated. It is demonstrated that a less negative charge on the Bi_2WO_6 photoanode layer at pH = 1 leads to the significant improvement in the overall energy conversion in DSSCs. The measured photocurrent−voltage properties obviously indicated that the mixture of Bi_2WO_6 and TiO_2 nanoparticles exhibited considerably improved photocurrent

https://doi.org/10.1021/acs.iecr.1c01812
Ind. Eng. Chem. Res. 2021, 60, 12292−12306

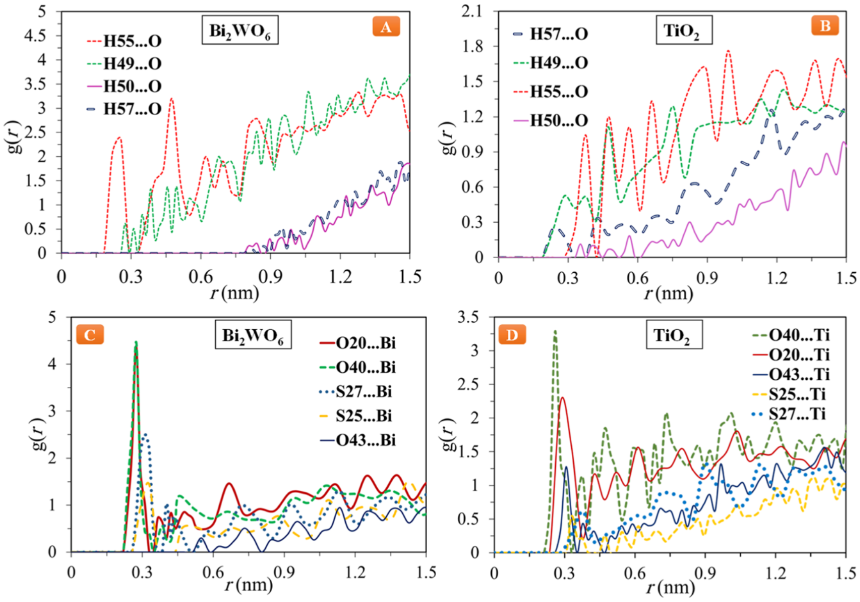

Figure 12. RDFs of hydrogen atoms of N719 dye with the Bi_2WO_6 surface (A) and with TiO_2 surface(B) and RDFs of oxygen and sulfur atoms of N719 dye with the Bi_2WO_6 surface (C) and with TiO_2 surface (D) (see Scheme 2 for the atom labeling).

Table 6. Diffusion Coefficients ⟨*D*⟩ (10^{-10} $m^2 \cdot s^{-1}$) of Dye Solution Components Obtained from the MSD-Time Curves in the *NVT* Ensemble

system	ethanol	N719
bulk (dye solution)	3.64	0.70
Bi_2WO_6	15.53	4.90
TiO_2	9.31	3.26

density (J_{sc}), as compared to the pure Bi_2WO_6 devices, which consequently provides a much increased conversion efficiency. The main reasons for better performance of TiO_2 solar cells in comparison with Bi_2WO_6 solar cells were investigated through MD simulation studies, in terms of electrolyte solution interactions with surfaces and also dye molecule distribution on the TiO_2 and Bi_2WO_6 surfaces. The density profile and RDF plots indicated that Li^+ ions were mainly accumulated at the Bi_2WO_6 surface, while the I^- ions had significant correlations with the TiO_2 surface. Interestingly, as a result of the interactions between ions and solid surfaces, the dynamics of ions were reduced when the electrolyte solution was confined between solid surfaces. The simulation results indicated that N719 dye molecules were adsorbed in the Stern layer at the TiO_2 surface, while these dye molecule were placed in the second layer (diffuse layer) after a tightly bound ethanol layer in the Bi_2WO_6 system.

■ ASSOCIATED CONTENT

Supporting Information

The Supporting Information is available free of charge at https://pubs.acs.org/doi/10.1021/acs.iecr.1c01812.

Cross-sectional SEM image of the Bi_2WO_6 film, RDFs, mean-square displacement, and calculated RDF–distances (PDF)

■ AUTHOR INFORMATION

Corresponding Authors

Amin Reza Zolghadr − *Department of Chemistry, Shiraz University, Shiraz 71946-84795, Iran*; orcid.org/0000-0002-6289-3794; Phone: +98 713 613 7157; Email: arzolghadr@shirazu.ac.ir; Fax: +98 713 646 0788

Hadi Salari − *Department of Chemistry, Shiraz University, Shiraz 71946-84795, Iran*; orcid.org/0000-0001-8809-3480; Email: hsalari@shirazu.ac.ir

Authors

Omid Estakhr − *Department of Chemistry, Shiraz University, Shiraz 71946-84795, Iran*

Maryam Heydari Dokoohaki − *Department of Chemistry, Shiraz University, Shiraz 71946-84795, Iran*

Complete contact information is available at: https://pubs.acs.org/10.1021/acs.iecr.1c01812

Author Contributions

A.R.Z and H.S are co-first authors.

Notes

The authors declare no competing financial interest.

■ ACKNOWLEDGMENTS

The authors are indebted to the research council of the Shiraz University for financial supports.

■ REFERENCES

(1) Sánchez, A. S.; Torres, E. A.; Kalid, R. A. Renewable energy generation for the rural electrification of isolated communities in the Amazon Region. *Renewable Sustainable Energy Rev.* **2015**, *49*, 278−290.

(2) Kabir, E.; Kumar, P.; Kumar, S.; Adelodun, A. A.; Kim, K.-H. Solar energy: Potential and future prospects. *Renewable Sustainable Energy Rev.* **2018**, *82*, 894−900.

(3) Foster, R.; Ghassemi, M.; Cota, A. *Solar Energy: Renewable Energy and the Environment*; CRC Press, 2009.

(4) Hagfeldt, A.; Boschloo, G.; Sun, L.; Kloo, L.; Pettersson, H. Dye-sensitized solar cells. *Chem. Rev.* **2010**, *110*, 6595−6663.

(5) Lee, S. H.; Kwon, J.; Kim, D. Y.; Song, K.; Oh, S. H.; Cho, J.; Schubert, E. F.; Park, J. H.; Kim, J. K. Enhanced power conversion efficiency of dye-sensitized solar cells with multifunctional photoanodes based on a three-dimensional TiO_2 nanohelix array. *Sol. Energy Mater. Sol. Cells* **2015**, *132*, 47−55.

(6) Liu, G.; Zhao, Y.; Wang, K.; He, D.; Yao, R.; Li, J. Ultrasmall NiFe-phosphate nanoparticles incorporated α-Fe_2O_3 nanoarrays photoanode realizing high efficient solar water splitting. *ACS Sustainable Chem. Eng.* **2018**, *6*, 2353−2361.

(7) O'regan, B.; Grätzel, M. A low-cost, high-efficiency solar cell based on dye-sensitized colloidal TiO_2 films. *Nature* **1991**, *353*, 737−740.

(8) Wang, J.; Bai, F.-Q.; Xia, B.-H.; Feng, L.; Zhang, H.-X.; Pan, Q.-J. On the viability of cyclometalated Ru(ii) complexes as dyes in DSSC regulated by COOH group, a DFT study. *Phys. Chem. Chem. Phys.* **2011**, *13*, 2206−2213.

(9) Tercan, M.; Dayan, O. Synthesis and DSSC applications of Ru (II) complexes bearing benzimidazole type ligands. *J. Electron. Mater.* **2019**, *48*, 642−648.

(10) Drygała, A. Influence of TiO_2 film thickness on photovoltaic properties of dye-sensitized solar cells. *IOP Conference Series: Earth and Environmental Science*; IOP Publishing, 2021; p 012001.

(11) Nazeeruddin, M. K.; De Angelis, F.; Fantacci, S.; Selloni, A.; Viscardi, G.; Liska, P.; Ito, S.; Takeru, B.; Grätzel, M. Combined experimental and DFT-TDDFT computational study of photoelectrochemical cell ruthenium sensitizers. *J. Am. Chem. Soc.* **2005**, *127*, 16835−16847.

(12) Nazeeruddin, M. K.; Kay, A.; Rodicio, I.; Humphry-Baker, R.; Müller, E.; Liska, P.; Vlachopoulos, N.; Grätzel, M. Conversion of light to electricity by cis-X_2bis (2, 2'-bipyridyl-4, 4'-dicarboxylate) ruthenium (II) charge-transfer sensitizers (X= Cl-, Br-, I-, CN-, and SCN-) on nanocrystalline titanium dioxide electrodes. *J. Am. Chem. Soc.* **1993**, *115*, 6382−6390.

(13) De Angelis, F.; Fantacci, S.; Mosconi, E.; Nazeeruddin, M. K.; Grätzel, M. Absorption Spectra and Excited State Energy Levels of the N719 Dye on TiO_2 in Dye-Sensitized Solar Cell Models. *J. Phys. Chem. C* **2011**, *115*, 8825−8831.

(14) Lan, J.-L.; Wei, T.-C.; Feng, S.-P.; Wan, C.-C.; Cao, G. Effects of iodine content in the electrolyte on the charge transfer and power conversion efficiency of dye-sensitized solar cells under low light intensities. *J. Phys. Chem. C* **2012**, *116*, 25727−25733.

(15) Boschloo, G.; Gibson, E. A.; Hagfeldt, A. Photomodulated voltammetry of iodide/triiodide redox electrolytes and its relevance to dye-sensitized solar cells. *J. Phys. Chem. Lett.* **2011**, *2*, 3016−3020.

(16) Kelly, C. A.; Farzad, F.; Thompson, D. W.; Stipkala, J. M.; Meyer, G. J. Cation-Controlled Interfacial Charge Injection in Sensitized Nanocrystalline TiO_2. *Langmuir* **1999**, *15*, 7047−7054.

(17) Li, R.; Liu, D.; Zhou, D.; Shi, Y.; Wang, Y.; Wang, P. Influence of the electrolyte cation in organic dye-sensitized solar cells: lithium versus dimethylimidazolium. *Energy Environ. Sci.* **2010**, *3*, 1765−1772.

(18) Taya, S.; Kuwahara, S.; Shen, Q.; Toyoda, T.; Katayama, K. Role of lithium and co-existing cations in electrolyte to improve performance of dye-sensitized solar cells. *RSC Adv.* **2014**, *4*, 21517−21520.

(19) Bandara, T. M. W. J.; Fernando, H. D. N. S.; Furlani, M.; Albinsson, I.; Dissanayake, M. A. K. L.; Ratnasekera, J. L.; Mellander, B.-E. Dependence of solar cell performance on the nature of alkaline counterion in gel polymer electrolytes containing binary iodides. *J. Solid State Electrochem.* **2017**, *21*, 1571−1578.

(20) Teo, L. P.; Tiong, T. S.; Buraidah, M. H.; Arof, A. K. Effect of lithium iodide on the performance of dye sensitized solar cells (DSSC) using poly(ethylene oxide) (PEO)/poly(vinyl alcohol) (PVA) based gel polymer electrolytes. *Opt. Mater.* **2018**, *85*, 531−537.

(21) Ko, S. H.; Lee, D.; Kang, H. W.; Nam, K. H.; Yeo, J. Y.; Hong, S. J.; Grigoropoulos, C. P.; Sung, H. J. Nanoforest of hydrothermally grown hierarchical ZnO nanowires for a high efficiency dye-sensitized solar cell. *Nano Lett.* **2011**, *11*, 666−671.

(22) DiMarco, B. N.; Sampaio, R. N.; James, E. M.; Barr, T. J.; Bennett, M. T.; Meyer, G. J. Efficiency Considerations for SnO_2-Based Dye-Sensitized Solar Cells. *ACS Appl. Mater. Interfaces* **2020**, *12*, 23923−23930.

(23) Le Viet, A.; Jose, R.; Reddy, M. V.; Chowdari, B. V. R.; Ramakrishna, S. Nb_2O_5 photoelectrodes for dye-sensitized solar cells: choice of the polymorph. *J. Phys. Chem. C* **2010**, *114*, 21795−21800.

(24) Yi, Z.; Zeng, Y.; Wu, H.; Chen, X.; Fan, Y.; Yang, H.; Tang, Y.; Yi, Y.; Wang, J.; Wu, P. Synthesis, surface properties, crystal structure and dye-sensitized solar cell performance of TiO_2 nanotube arrays anodized under different parameters. *Results Phys.* **2019**, *15*, 102609.

(25) Shakeel Ahmad, M.; Pandey, A. K.; Abd Rahim, N. Advancements in the development of TiO_2 photoanodes and its fabrication methods for dye sensitized solar cell (DSSC) applications. A review. *Renewable Sustainable Energy Rev.* **2017**, *77*, 89−108.

(26) Umale, S.; Sudhakar, V.; Sontakke, S. M.; Krishnamoorthy, K.; Pandit, A. B. Improved efficiency of DSSC using combustion synthesized TiO_2. *Mater. Res. Bull.* **2019**, *109*, 222−226.

(27) Wu, R.; Song, H.; Luo, N.; Sheng, Y.; Ji, G. Microwave-assisted preparation and enhanced photocatalytic activity of Bi_2WO_6/BiOI heterojunction for organic pollutants degradation under visible-light irradiation. *Solid State Sci.* **2019**, *87*, 101−109.

(28) Arif, M.; Min, Z.; Yuting, L.; Yin, H.; Liu, X. A Bi_2WO_6-based hybrid heterostructures photocatalyst with enhanced photodecomposition and photocatalytic hydrogen evolution through Z-scheme process. *J. Ind. Eng. Chem.* **2019**, *69*, 345−357.

(29) Sun, C.; Wang, Y.; Su, Q. Sol-gel synthesis of Bi_2WO_6/graphene thin films with enhanced photocatalytic performance for nitric monoxide oxidation under visible light irradiation. *Chem. Phys. Lett.* **2018**, *702*, 49−56.

(30) Hoang, L. H.; Phu, N. D.; Peng, H.; Chen, X.-B. High photocatalytic activity N-doped Bi_2WO_6 nanoparticles using a two-step microwave-assisted and hydrothermal synthesis. *J. Alloys Compd.* **2018**, *744*, 228−233.

(31) Hu, S.-P.; Xu, C.-Y.; Zhen, L. Solvothermal synthesis of Bi_2WO_6 hollow structures with excellent visible-light photocatalytic properties. *Mater. Lett.* **2013**, *95*, 117−120.

(32) Hu, S.-P.; Xu, C.-Y.; Wang, W.-S.; Ma, F.-X.; Zhen, L. Synthesis of Bi_2WO_6 hierarchical structures constructed by porous nanoplates and their associated photocatalytic properties under visible light irradiation. *Ceram. Int.* **2014**, *40*, 11689−11698.

(33) Zhang, L.; Wang, H.; Chen, Z.; Wong, P. K.; Liu, J. Bi_2WO_6 micro/nano-structures: synthesis, modifications and visible-light-driven photocatalytic applications. *Appl. Catal., B* **2011**, *106*, 1−13.

(34) Rapaport, D. C. *The Art of Molecular Dynamics Simulation*; Cambridge University Press, 2004.

(35) Mohammadpour, F.; Heydari Dokoohaki, M.; Zolghadr, A. R.; Ghatee, M. H.; Moradi, M. Confinement of aqueous mixtures of ionic liquids between amorphous TiO_2 slit nanopores: electrostatic field induction. *Phys. Chem. Chem. Phys.* **2018**, *20*, 29493−29502.

(36) Wu, P.; Huang, J.; Meunier, V.; Sumpter, B. G.; Qiao, R. Complex capacitance scaling in ionic liquids-filled nanopores. *ACS Nano* **2011**, *5*, 9044−9051.

(37) Sawatsuk, T.; Chindaduang, A.; Sae-Kung, C.; Pratontep, S.; Tumcharern, G. Dye-sensitized solar cells based on TiO_2−MWCNTs composite electrodes: Performance improvement and their mechanisms. *Diamond Relat. Mater.* **2009**, *18*, 524−527.

(38) Frisch, M.; Trucks, G.; Schlegel, H.; Scuseria, G.; Robb, M.; Cheeseman, J.; Scalmani, G.; Barone, V.; Mennucci, B.; Petersson, G. *Gaussian 09*; Gaussian, Inc.: Wallingford CT, 2009.

(39) Hay, P. J.; Wadt, W. R. Ab initio effective core potentials for molecular calculations. Potentials for the transition metal atoms Sc to Hg. *J. Chem. Phys.* **1985**, *82*, 270−283.

(40) Reed, A. E.; Curtiss, L. A.; Weinhold, F. Intermolecular interactions from a natural bond orbital, donor-acceptor viewpoint. *Chem. Rev.* **1988**, *88*, 899−926.

(41) Pronk, S.; Páll, S.; Schulz, R.; Larsson, P.; Bjelkmar, P.; Apostolov, R.; Shirts, M. R.; Smith, J. C.; Kasson, P. M.; van der Spoel, D.; Hess, B.; Lindahl, E. GROMACS 4.5: a high-throughput

https://doi.org/10.1021/acs.iecr.1c01812
Ind. Eng. Chem. Res. 2021, 60, 12292−12306

and highly parallel open source molecular simulation toolkit. *Bioinformatics* **2013**, *29*, 845−854.
(42) Singh, R.; Rajput, N. N.; He, X.; Monk, J.; Hung, F. R. Molecular dynamics simulations of the ionic liquid [$EMIM^+$]-[$TFMSI^-$] confined inside rutile (110) slit nanopores. *Phys. Chem. Chem. Phys.* **2013**, *15*, 16090−16103.
(43) Heinz, H.; Vaia, R. A.; Farmer, B. L.; Naik, R. R. Accurate simulation of surfaces and interfaces of face-centered cubic metals using 12− 6 and 9− 6 Lennard-Jones potentials. *J. Phys. Chem. C* **2008**, *112*, 17281−17290.
(44) Maulana, A.; Su'ud, Z.; Hermawan, K D. Simulation study of steels corrosion phenomenon in liquid lead−bismuth cooled reactors using molecular dynamics methods. *Prog. Nucl. Energy* **2008**, *50*, 616−620.
(45) Bernardes, C. E. S.; Canongia Lopes, J. N.; da Piedade, M. E. M. All-atom force field for molecular dynamics simulations on organotransition metal solids and liquids. Application to M (CO) n (M= Cr, Fe, Ni, Mo, Ru, or W) compounds. *J. Phys. Chem. A* **2013**, *117*, 11107−11113.
(46) Rappé, A. K.; Casewit, C. J.; Colwell, K. S.; Goddard, W. A., III; Skiff, W. M. UFF, a full periodic table force field for molecular mechanics and molecular dynamics simulations. *J. Am. Chem. Soc.* **1992**, *114*, 10024−10035.
(47) Azpiroz, J. M.; De Angelis, F. DFT/TDDFT Study of the Adsorption of N3 and N719 Dyes on ZnO(101¯0) Surfaces. *J. Phys. Chem. A* **2014**, *118*, 5885−5893.
(48) Bussi, G.; Donadio, D.; Parrinello, M. Canonical sampling through velocity rescaling. *J. Chem. Phys.* **2007**, *126*, 014101.
(49) Wu, J.; Duan, F.; Zheng, Y.; Xie, Y. Synthesis of Bi_2WO_6 nanoplate-built hierarchical nest-like structures with visible-light-induced photocatalytic activity. *J. Phys. Chem. C* **2007**, *111*, 12866−12871.
(50) Li, J.-d.; Yu, C.-l.; Fang, W.; Zhu, L.-h.; Zhou, W.-q.; Fan, Q.-z. Preparation, characterization and photocatalytic performance of heterostructured $AgCl/Bi_2WO_6$ microspheres. *Chin. J. Catal.* **2015**, *36*, 987−993.
(51) Tahmasebi, N.; Maleki, Z.; Farahnak, P. Enhanced photocatalytic activities of Bi_2WO_6/BiOCl composite synthesized by one-step hydrothermal method with the assistance of HCl. *Mater. Sci. Semicond. Process.* **2019**, *89*, 32−40.
(52) Cao, X.-F.; Zhang, L.; Chen, X.-T.; Xue, Z.-L. Microwave-assisted solution-phase preparation of flower-like Bi_2WO_6 and its visible-light-driven photocatalytic properties. *CrystEngComm* **2011**, *13*, 306−311.
(53) Bardestani, R.; Patience, G. S.; Kaliaguine, S. Experimental methods in chemical engineering: specific surface area and pore size distribution measurements-BET, BJH, and DFT. *Can. J. Chem. Eng.* **2019**, *97*, 2781−2791.
(54) Zhu, Z.; Yan, Y.; Li, J. One-step synthesis of flower-like WO_3/Bi_2WO_6 heterojunction with enhanced visible light photocatalytic activity. *J. Mater. Sci.* **2016**, *51*, 2112−2120.
(55) Salari, H.; Yaghmaei, H. Z-scheme 3D Bi_2WO_6/MnO_2 heterojunction for increased photoinduced charge separation and enhanced photocatalytic activity. *Appl. Surf. Sci.* **2020**, *532*, 147413.
(56) Salari, H. Facile template-free synthesis of 3D flower-like Bi_2WO_6/MoO_3 nanocomposites with ultra-thin sheets and their associated photocatalytic properties under visible light irradiation. *J. Photochem. Photobiol., A* **2019**, *385*, 112069.
(57) Kohantorabi, M.; Giannakis, S.; Gholami, M. R. Supported PtxPd1-x bimetallic nanoparticles on ionic liquid-functionalized SiO_2@ graphene oxide nanocomposite and its application as an effective multiphasic catalyst. *Appl. Catal., A* **2019**, *579*, 30−43.
(58) Jia-Yi, S.; Xiao-Jin, L.; Yi-Ming, X. Effect of sintering temperature on the photocatalytic activity of flower-like Bi_2WO_6. *Acta Phys.-Chim. Sin.* **2014**, *30*, 508−512.
(59) Huang, Y.; Zhang, X.; Zhou, Z.; Shen, S. A new and facile co-modification by introducing oxygen vacancies and loading Ag nanoparticles to promote the photocatalytic activities of Bi_2WO_6. *Mater. Res. Bull.* **2019**, *119*, 110538.
(60) Salari, H.; Kohantorabi, M. Fabrication of novel Fe_2O_3/MoO_3/AgBr nanocomposites with enhanced photocatalytic activity under visible light irradiation for organic pollutant degradation. *Adv. Powder Technol.* **2020**, *31*, 493−503.
(61) Miao, C.; Chen, C.; Dai, Q.; Xu, L.; Song, H. Dysprosium, holmium and erbium ions doped indium oxide nanotubes as photoanodes for dye sensitized solar cells and improved device performance. *J. Colloid Interface Sci.* **2015**, *440*, 162−167.
(62) Thavasi, V.; Renugopalakrishnan, V.; Jose, R.; Ramakrishna, S. Controlled electron injection and transport at materials interfaces in dye sensitized solar cells. *Mater. Sci. Eng., R* **2009**, *63*, 81−99.
(63) Zhang, X.; Zhang, L.; Xie, T.; Wang, D. Low-Temperature Synthesis and High Visible-Light-Induced Photocatalytic Activity of $BiOI/TiO_2$ Heterostructures. *J. Phys. Chem. C* **2009**, *113*, 7371−7378.
(64) Li, Z.-Q.; Chen, X.-T.; Xue, Z.-L. Microwave-assisted synthesis and photocatalytic properties of flower-like Bi2WO6 and Bi_2O_3−Bi_2WO_6 composite. *J. Colloid Interface Sci.* **2013**, *394*, 69−77.
(65) Liu, T.-C.; Wu, C.-C.; Huang, C.-H.; Chen, C.-M. Effects of ethyl cellulose on performance of titania photoanode for dye-sensitized solar cells. *J. Electron. Mater.* **2016**, *45*, 6192−6199.
(66) Dervaux, J.; Cormier, P.-A.; Konstantinidis, S.; Di Ciuccio, R.; Coulembier, O.; Dubois, P.; Snyders, R. Deposition of porous titanium oxide thin films as anode material for dye sensitized solar cells. *Vacuum* **2015**, *114*, 213−220.
(67) Sengupta, D.; Das, P.; Mondal, B.; Mukherjee, K.; Reviews, S. E. Effects of doping, morphology and film-thickness of photo-anode materials for dye sensitized solar cell application−A review. *Renewable Sustainable Energy Rev.* **2016**, *60*, 356−376.
(68) Wu, J.-J.; Chen, G.-R.; Lu, C.-C.; Wu, W.-T.; Chen, J.-S. Performance and electron transport properties of TiO_2 nanocomposite dye-sensitized solar cells. *Nanotechnology* **2008**, *19*, 105702.
(69) Yu, J.; Fan, J.; Zhao, L. Dye-sensitized solar cells based on hollow anatase TiO_2 spheres prepared by self-transformation method. *Electrochim. Acta* **2010**, *55*, 597−602.
(70) Wang, Z.; Tang, Y.; Li, M.; Zhu, Y.; Li, M.; Bai, L.; Luoshan, M.; Lei, W.; Zhao, X. Compounds, Plasmonic enhancement of the performance of dye-sensitized solar cells by incorporating TiO_2 nanotubes decorated with Au nanoparticles. *J. Alloys Compd.* **2017**, *714*, 89−95.
(71) Marandi, M.; Anajafi, Z.; Naeimi Sani Sabet, M.; Bayat, S. Fabrication of dye sensitized solar cells with improved multi-layer photonodes of hydrothermally grown TiO_2 nanocrystals in different autoclaving pHs. *J. Mater. Sci.: Mater. Electron.* **2017**, *28*, 9548−9558.